Classification of underwater photogrammetry data for temperate benthic rocky reef mapping

Quentin Ternon, Valentin Danet, Pierre D Thiriet, Frédéric Ysnel, Eric Feunteun, Antoine Collin

Classification of underwater photogrammetry data for temperate benthic rocky reef mapping

Q. Ternon[a,b], V. Danet[a], P. Thiriet[c], F. Ysnel[d], E. Feunteun[a,b], A. Collin[e]

[a] Museum National d'Histoire Naturelle (MNHN), Station Marine de Dinard, Centre de Recherche et d'Enseignement sur les Systèmes CÔtiers (CRESCO), 35800, Dinard, France

[b] Laboratoire Biologie des Organismes et Écosystèmes Aquatiques (UMR BOREA), MNHN, CNRS, Sorbonne Université, Université de Caen Normandie, Université des Antilles, IRD, 75231, Paris Cedex, France

[c] UMS Patrimoine Naturel, OFB, CNRS, MNHN, CRESCO, 35800, Dinard, France

[d] Université de Rennes 1, UMR BOREA, MNHN, 35042, Rennes Cedex, France

[e] Ecole Pratique des Hautes Etudes (EPHE), PSL Université de recherche, CNRS UMR LETG, 35800, Dinard, France

Corresponding Author:

Quentin TERNON: quentin.ternon@mnhn.fr

MNHN-CRESCO, 38 rue du Port blanc, 35800, DINARD, France

Others Authors:

Valentin DANET: valentin.danet@mnhn.fr

Frederic YSNEL: frederic.ysnel@univ-rennes1.fr

Éric FEUNTEUN: eric.feunteun@mnhn.fr

Pierre THIRIET: pierre.thiriet@mnhn.fr

Antoine COLLIN: antoine.collin@ephe.psl.eu

Authors agreement to the submission

All authors declare being agree to the submission

Other specifications

Colour should be used for Fig. 1, 2, 4 and 6, and is recommended for Fig. 3, 5 and 8 and table 2 and 3.

Abstract

The fine characterization of the substrate is a baseline to thoroughly investigate the relations between organisms and their biotopes. Cutting edge spatial technologies now provide access to accurate information on biotopes and biocenoses both in terrestrial and in marine environments. Photogrammetry is one of them and has recently been applied in submarine environments especially in shallow clear water. In this study, we investigated the potential of photogrammetry to characterize benthic habitats in turbid environments. Although more challenging, turbid environments are more frequent in temperate marine coastal areas. We selected two rocky sites in the bay of Saint-Malo (Brittany, France), differentiated by their level of turbidity, one being a marine site exposed to natural tides (Buharats), while the other (Bizeux) is subjected to both natural tides and artificial currents created by the functioning of a hydroelectric dam. The different substrates observed were classified into eight classes at a centimetre resolution using photogrammetry-based spatial and multispectral predictors. The spatial benthic terrain predictors were derived from a digital surface model (DSM) at various spatial scales, and the multispectral predictors were retrieved from the red-green-blue (RGB, natural colours) orthomosaic imagery. An overall classification was computed for Buharats and Bizeux, with accuracies of 84.76 % and 79.54 % respectively, revealing a good quality of the substrate classification. The combination of RGB, DSM, and several spatial benthic terrain variables, with a pixel resolution of 5 and 10 mm, and a kernel size of 30, 60 and 90 pixels leads to the best benthic substrate classification (highest overall accuracy). At the class scale, producer's (PA) and user's (UA) accuracy showed that big boulders and field material were correctly distinguished. Small boulders and cobbles, having similar sizes, showed the lowest classification performances. This classification methodology provides new perspectives for

mesoscale (100 m² to 1 km²) semi-automatic mapping of the fine resolution (1 cm) relationship between benthic organisms and their substrate.

Key words

Photogrammetry; Temperate rocky reefs; Turbid water; Classification; Terrain variables; Substrate mapping

Author contributions

Quentin Ternon, Éric Feunteun, Frédéric Ysnel, Pierre Thiriet and Antoine Collin developed the study approach.

Quentin Ternon and Valentin Danet collected the data.

Quentin Ternon and Antoine Collin conducted the data analysis.

Quentin Ternon wrote the paper.

All authors participated to the manuscript revision.

Antoine Collin supervised the research.

1. Introduction

Substrate characteristics are known to control marine benthic communities specific composition and abundance. Reviews have recently highlighted a range of geomorphometric variables that could influence at various scales the descriptive parameters of sub-tidal rocky habitat communities (algae, invertebrates and fishes) both in tropical and temperate sub-tidal environments (Pygas et al., 2020 ; Borland et al., 2021). More particularly, the terrain complexity (e.g. rugosity, bathymetric variance and slope of the slope), its morphology (curvature and aspect), the substrate type (nature, features and engineer species) and other information (bathymetry and slope) have an influence on the presence, abundance, cover and diversity of algae and sessile invertebrates both in tropical (Duckworth, 2016), subtropical (Holmes et al., 2008; Zavalas et al., 2014, Bravo et al., 2020) and temperate environments (Castric-Fey et al., 1973, Castric-Fey and Chasse, 1991; Guinan et al., 2009; Elvenes et al., 2014). Studies have demonstrated that the terrain complexity is one of the key-factor strongly structurating the fish communities on tropical (Kuffner et al., 2007; Pittman et al., 2007; Pittman et al., 2009; Knudby et al., 2010; Pittman and Brown, 2011; Sekund and Pittman, 2017), subtropical (Moore et al., 2009; Monk et al., 2010; Moore et al., 2010; Monk et al., 2011; Coleman et al., 2016; Rees et al., 2018; Williams et al., 2019), and temperate reefs (Cameron et al., 2014). Therefore, the accurate characterisation of the substrate has the potential to provide a precise understanding of the relationship between sessile organisms and their substrate. For instance, this substrate-based information can be used to predict benthic community compositions (Rattray et al., 2009; Collin et al., 2011).

The development of novel mapping technologies such as satellite, LiDAR and acoustic tools now allow to fine-tune at various scales the characterisation of benthic

96 and demersal habitats in relation with community composition (Fig. 1). Although, these
97 technologies are currently able to define the substrate at macroscale (>1 km²), with
98 high spatial resolution (~10 cm through acoustic, ~1 m through LiDAR and Satellite),
99 LIDAR and satellite technologies are limited to the first 50 m of depth in clear water

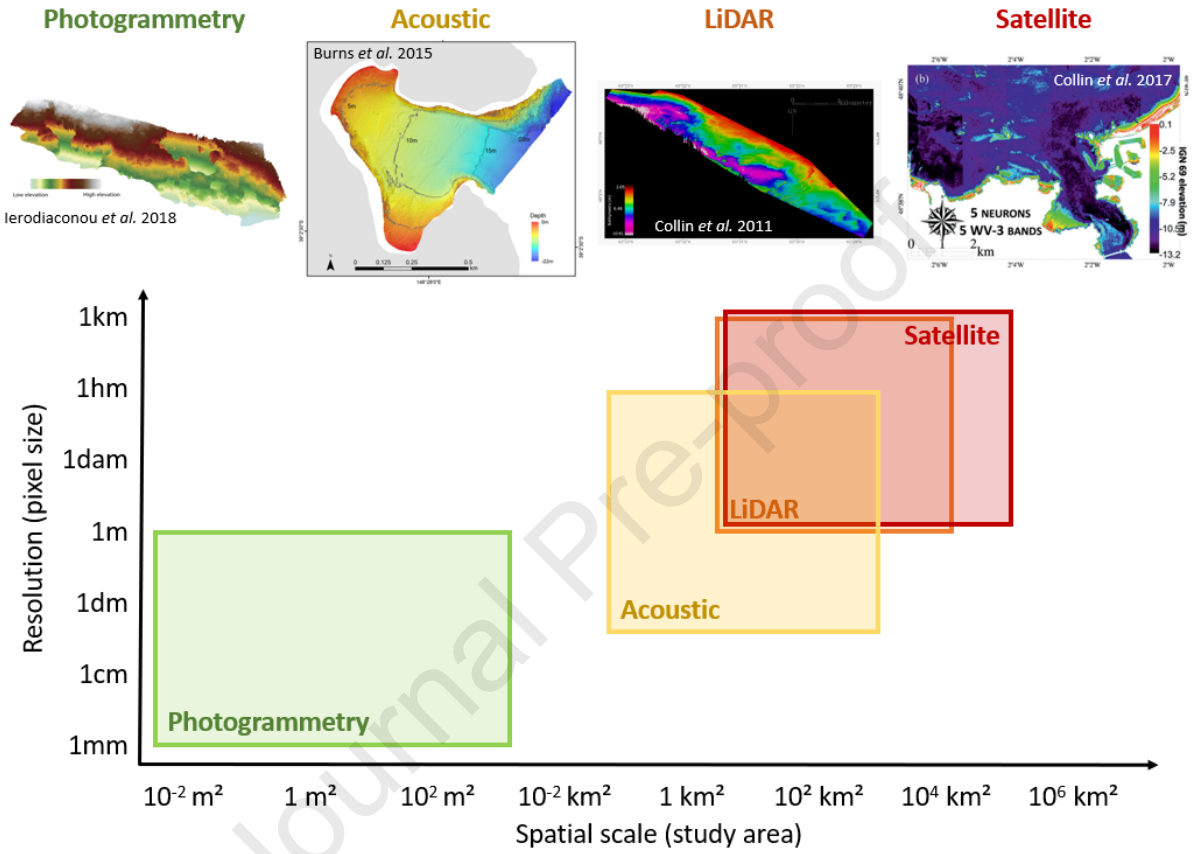

Fig. 1. The different techniques for benthic substrate imagery, their scope and performances. For each methodology, the limits of the rectangle indicate the range of spatial scale (horizontal) and resolution (vertical), and illustrations of benthic substrate imageries are given at the top of the diagram (data Irish and Lillycrop, 1999; Diaz et al., 2004; Bock et al., 2005; Collin et al., 2011; Knudby et al., 2011; Galparsoro, 2012; Collin et al., 2013; Dierssen and Theberge, 2014; Zavalas et al., 2014; Burns et al., 2015; Calvert et al., 2015; Smith et al., 2015; Wahidin et al., 2015; Ierodiaconou et al., 2018; Madricardo et al., 2019; Marre et al., 2019; Jackson et al., 2020; Marre et al., 2020a; Marre et al., 2020b).

because of water absorption (Irish and Lillycrop, 1999; Diaz et al., 2004; Bock et al., 2005; Collin et al., 2011; Knudby et al., 2011; Galparsoro, 2012; Collin et al. 2013; Dierssen and Theberge, 2014; Zavalas et al., 2014; Calvert et al., 2015; Smith et al., 2015; Wahidin et al., 2015; Ierodiaconou et al., 2018; Madricardo et al., 2019). LiDAR and sonar surveys can provide relevant information on the terrain characteristics, essential to describe and map benthic habitats (biotopes and biocenoses) (Pickrill and Todd, 2003; Collin et al., 2008; Pittman et al., 2009; Brown et al., 2011; Collin et al., 2011; Walbridge et al., 2018). Hence, this mapping constitutes an effective baseline to both target habitats of interest and evaluate the sampling effort required. More recently the photogrammetry technique has been developed and is now widely deployed in sub-tidal environments. This technique allows a 3D reconstruction with a more detailed characterisation of benthic rocky substrates and at larger scale of their associated landscapes (Hatcher et al., 2020). Based on multi-view optical information (either photographic or videographic), the photogrammetry has been mainly used in clear water environments to describe coral reefs structure at various biological levels from individuals to reefs (Burns et al., 2015; Figueira et al., 2015; Leon et al., 2015; Burns et al., 2016; Ferrari et al., 2016; Anelli et al., 2017; Carlot et al., 2020; Fukunaga et al., 2020). To date, this approach has been used to describe, up to a scale of 120 m^2 (mesoscale), the morphology of the substrate below a centimetre resolution (Fig. 1; Burns et al., 2015; Jackson et al., 2020; Marre et al., 2019; Marre, et al., 2020b). However, the substrate typology (i.e. bed rock, boulders, pebbles, gravel, sand), determinant for the structure and organisation of biological communities, has not been derived from photogrametry in these studies. There is currently a clear need to produce fine resolution (< 1 m) characterisations (geomorphology and typology) and maps of temperate rocky reefs, to better understand and monitor processes involved in habitat

dynamics as a response to environmental changes (Keith et al., 2020; see also European Commission and European Environment Agency). Additionally, testing the potential of photogrammetry applications in turbid water systems is lacking.

In this study, we propose an innovative method to produce a mesoscale (120 m^2) fine resolution (1 cm) classification of benthic substrates in turbid waters combining photogrammetry and supervised classification models. We selected two rocky temperate reefs, located in the bay of Saint Malo, France, with similar topographic features but characterised by different turbidity and hydrodynamic conditions. We analysed the ability of the supervised classification to detect and quantify the relative surface of eight substrate classes commonly used in the literature. A visual description of the transect landscape (distribution patterns of the substrate types) has been conducted to rapidly evaluate if differentiation of landscape patterns could be made. The contribution of the spatial (terrain) and multispectral (red-green-blue, RGB) predictors was investigated, and the best combination of predictors was statistically examined. This research aims to develop a classification method to spatially quantify the main biotope components of benthic rocky reef habitats.

2. Material and Methods

2.1. Study area

The sampling area is located in the English Channel in the St Malo Bay (Brittany, France). Two distinct rocky reef sites have been sampled by scuba-diving. The islet of Bizeux (48°37'40.95'' N, 2°01'34.96'' W; WGS84) is under the influence of natural tides, but also of functioning of the hydroelectric dam of the Rance, which create strong bidirectional currents and turbid episodes (Gallon et al., 2013). The second site, the

150 reef of Buharats (48°40'24.08" N, 2°07'12.88" W; WGS84) located 3 km offshore, is
151 more subject to marine influence but less turbid than Bizeux (Fig. 2).

152

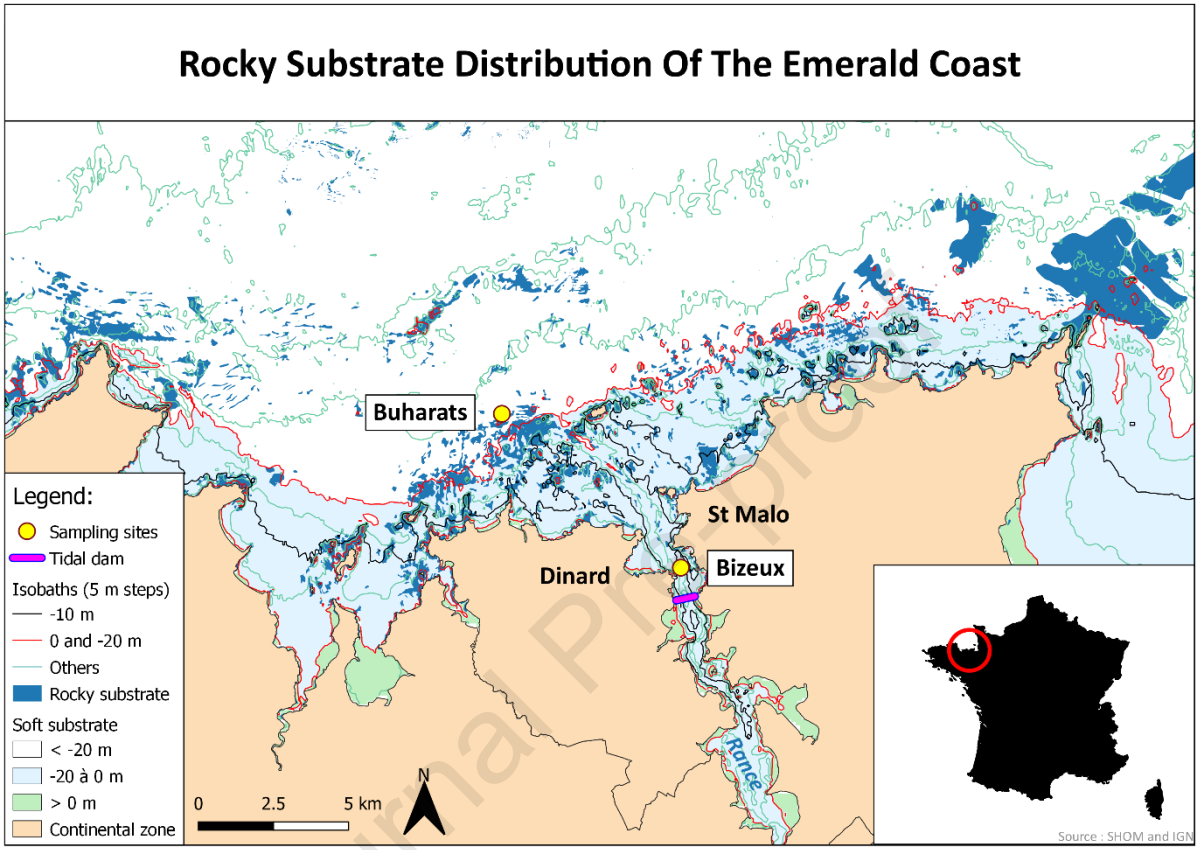

Fig. 2. Locations of the two sampling sites (Buharats and Bizeux) inside the rocky substrate distribution of the Emerald Coast. The different isobaths are displayed with a 5 m step.

153 For each reef, a 120 m² transect (30 m long and 4 m wide ; Fig. 3) was
154 investigated in circa-littoral habitats, under the kelp belts, at depths of 13 +/- 1 m (0 m
155 corresponding to the lowest astronomical tide level).

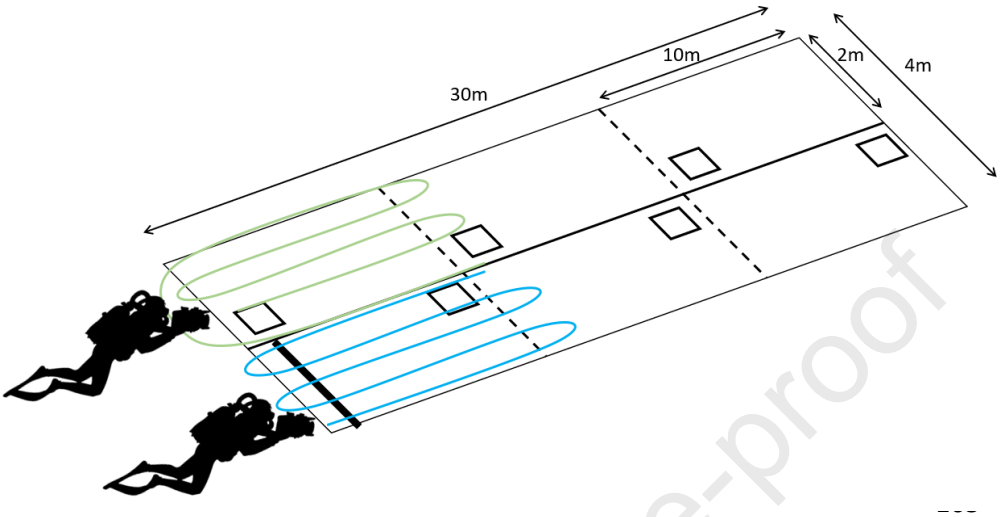

Fig. 3. Scheme of the 120 m² transect (30 m long and 4 m large) shooting. The dotted lines separate each 10 m sections. The curved lines symbolize the trajectory of divers in their respected lane during the sampling. The six squares indicate the position of quadrats (50 x 50 cm). The thick line indicates the 2 m rule.

166 ## 2.2. Imagery acquisition
167

168 A total of 1831 and 1995 pictures were taken for Bizeux and Buharats,
169 respectively (Fig. 3 and Fig. 4 step 1). The transect was set-out with a 30 m tape. Six
170 quadrats (0.25 m²) were distributed along the transect and a 2 m rule was placed for
171 an *a posteriori* calibration. Special photogrammetric markers were fixed on quadrats
172 (8 markers) and rules (6 markers) for the 3D model construction. The depth was
173 controlled with a dive computer (Suunto Vyper©, 10 cm precision). Each quadrat was
174 georeferenced (in latitude and longitude) under water using a submarine geolocation
175 system (i.e.

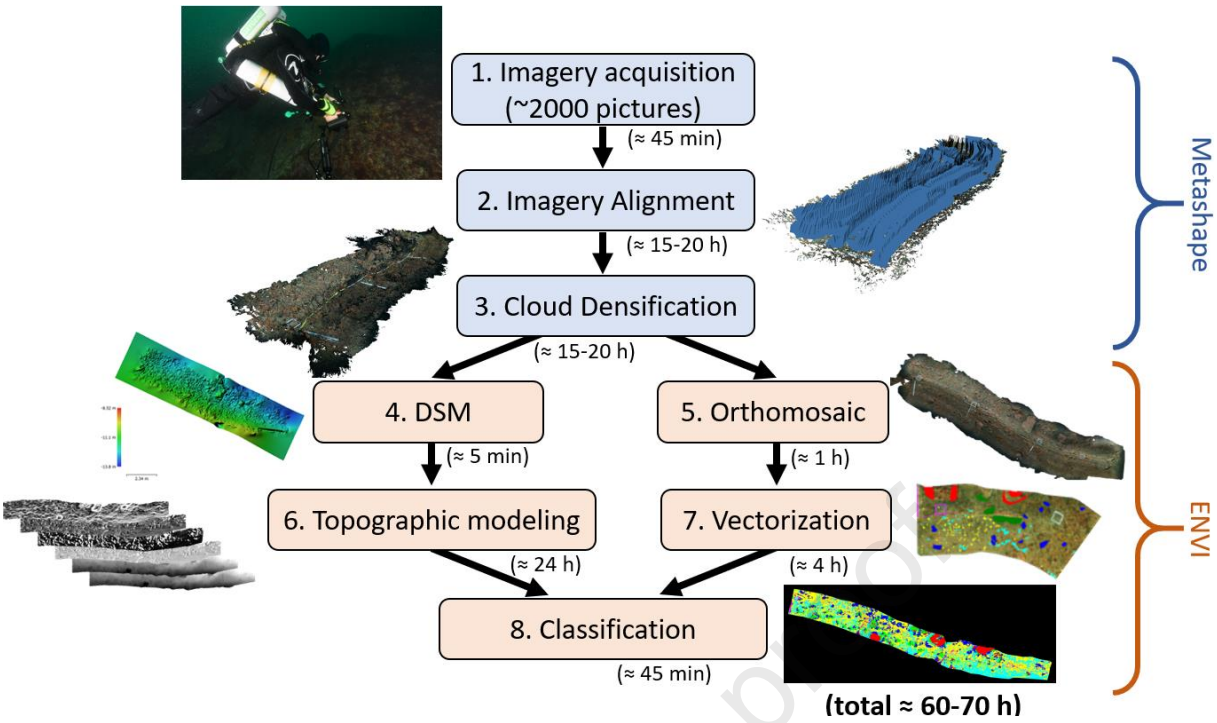

Fig. 4. Workflow of the photogrammetry to describe a 120 m^2 transect of benthic temperate rocky substrates from photograph acquisition to classification. The time indications represent the rough duration of each process. Software used to perform each process are indicated on the right. DSM: Digital surface model.

UWIS© system; 1m precision). The transect was divided in 2 lanes of 2 meters wide (one for each diver) and 3 consecutive sections of 10 m long (to secure data collection; Fig. 3). Digital single-lens reflex D7500-NIKON (set to 20.1 MegaPixel, F13, 1/250 s, ISO 400-800) with a 10-24 mm NIKON lens (set to 10 mm), placed in an ISOTA underwater housing, has been used for the multispectral imagery acquisition. Two PRO160-Subtronic strobes (set to 1/4 - 1/8 of the total power) were also used. Divers swam 1 m above the substrate and took pictures modulating their swimming speed and frequency of picture acquisition to ensure an approximately 60 % overlay between each photograph. Divers also maintained the camera roughly orthogonal to the substrate fitting as well as possible the shape of the substrate. An extra crossing was also carried on, with an oblique view, to improve the quality of the final model.

2.3. Photogrammetric model construction

All the process was performed using the Agisoft Metashape Software (version 1.6.1; see Table S1 for parametrization details), as frequently used in photogrammetry investigation (Burns et al., 2015; Leon et al., 2015; Bayley et al., 2019; Marre et al., 2019; Bayley and Mogg, 2020). Each lane was separated in 3 transversal segments in which a georeferenced quadrat was placed. In each segment, the markers were automatically detected and photographs were aligned. Chunks were then assembled based on markers having a new chunk with the assembled pictures of the whole transect (Fig. 4 step 2). A dense cloud process was then applied on the latter (Fig. 4 step 3). The coordinates (latitude, longitude, and depth) of each quadrat and the known distance of the 2 m rule were manually annotated (see Table S2 for details on error estimation of the 3D model). A digital surface model (hereafter DSM, free resolution) followed by an orthomosaic (fixed at a 1 mm resolution) process were then performed (Fig. 4 step 4 and 5).

2.4. Topographic modelling

The whole process was deployed under the ENVI Classic software (version 5.3). The DSM built from the photogrammetric model was first imported and resized to 5 and 10 mm pixel resolutions (r). A topographic modelling process was applied on the DSM band selecting 6 different benthic terrain variables : the slope, as the rate of change in elevation over horizontal distance between pixels in degree; the aspect, as the horizontal direction of the slope in degree; the profile and plan convexity, respectively as the vertical and horizontal components of the curvature without unit; the maximum curvature, as the largest local curvature in any direction without unit; the

212 root mean square error (RMSE), as the rate of change of the bathymetry in meters
213 (Fig. 4 step 6 and Fig. 5).

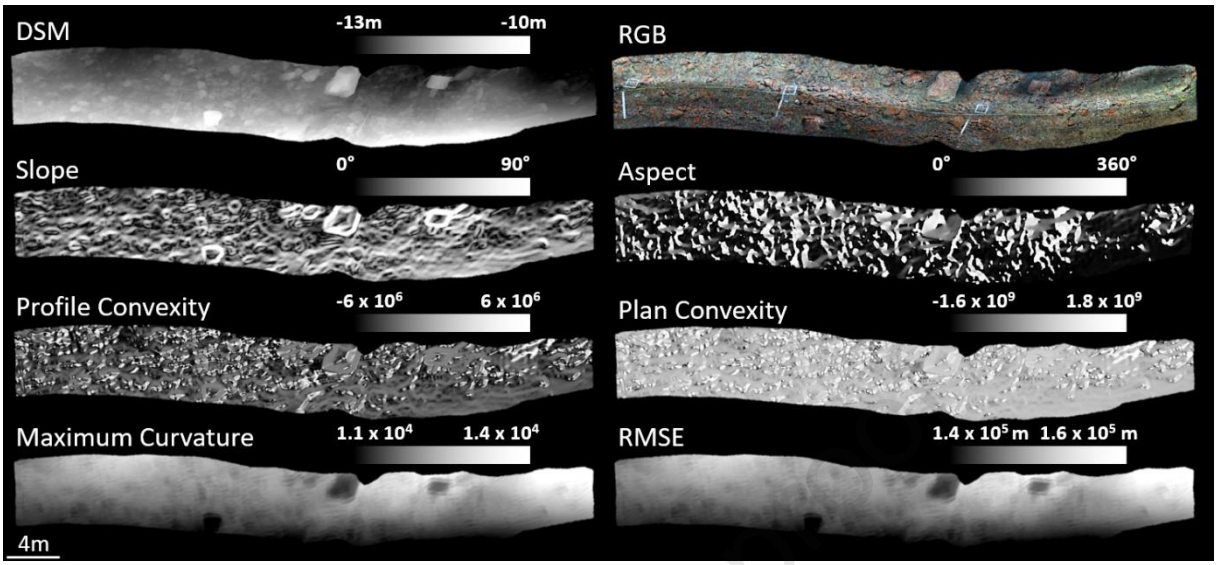

Fig.5. Pictures of the digital surface model (DSM), using average bathymetry in meters, for Bizeux (calculation window: k = 30 and r = 5 mm), orthomosaic combining red, green and blue (RGB) multispectral bands in digital numbers and the different terrain variables: the slope, aspect, profile convexity, plan convexity, maximum curvature, root mean square error (RMSE) (See details in 2.4 section).

214 These six variables were grouped under the term Terrain. Different combinations of
215 resolution (r) and kernel size (k) were used to obtain various size of calculation
216 windows for a multiscale approach (Table 1; Wilson et al., 2007; Porskamp et al.,
217 2018):

218 *Table 1: The different combinations of resolution (r) and kernel size (k) to obtain the different calculation windows*

Calculation window (in cm)	Kernel size (k, in pixel)	Resolution (r, in mm)
1.5	30	5
3	30	10
6	60	10
9	90	10

219

220

2.5. Model classification

A supervised classification is commonly used for typological mapping. Machine learners have been developed and widely used for benthic biotope classification (Collin et al., 2011; Hasan et al., 2014). However, some of them can suffer from a low transferability to people without specific machine learning skills. Moreover, these are not well suited for high frequency monitoring because of their complexity and also as they are computationally time consuming. Among various algorithms gleaned from the literature, the maximum likelihood classifier, based on the probabilistic membership, is described as a fast and highly transferable one (Pal and Mather, 2003; Collin et al., 2019; James et al., 2020a; James et al., 2020b). This algorithm is a pixel-wise method based on a Gaussian distribution of classes of interest. Pal and Mather (2003) defined it as the association of a pixel to a specific class if the probability of belonging to this class is higher than those of the other classes.

The orthomosaic based on multispectral information (RGB) was built from the photogrammetric model, and then imported and staked with the DSM and Terrain variables (all calculation windows). From the orthomosaic, different typological classes of the substrate (bed rock, big/medium/small boulder, cobble, pebble, sand and field material; Fig. 6) were visually identified (visual size estimation) and manually vectorized (Fig. 4 step 7). A threshold of a minimum of 1 000 000 pixels was reached for each class (500 000 for the field material class). Vectorized pixels were randomly subsampled in two sets of 500 000 pixels (250 000 for field material) respectively for the calibration and validation of the classification. A supervised classification process was applied using the maximum likelihood algorithm and the calibration pixel set (Fig. 4 step 8 and 6).

246

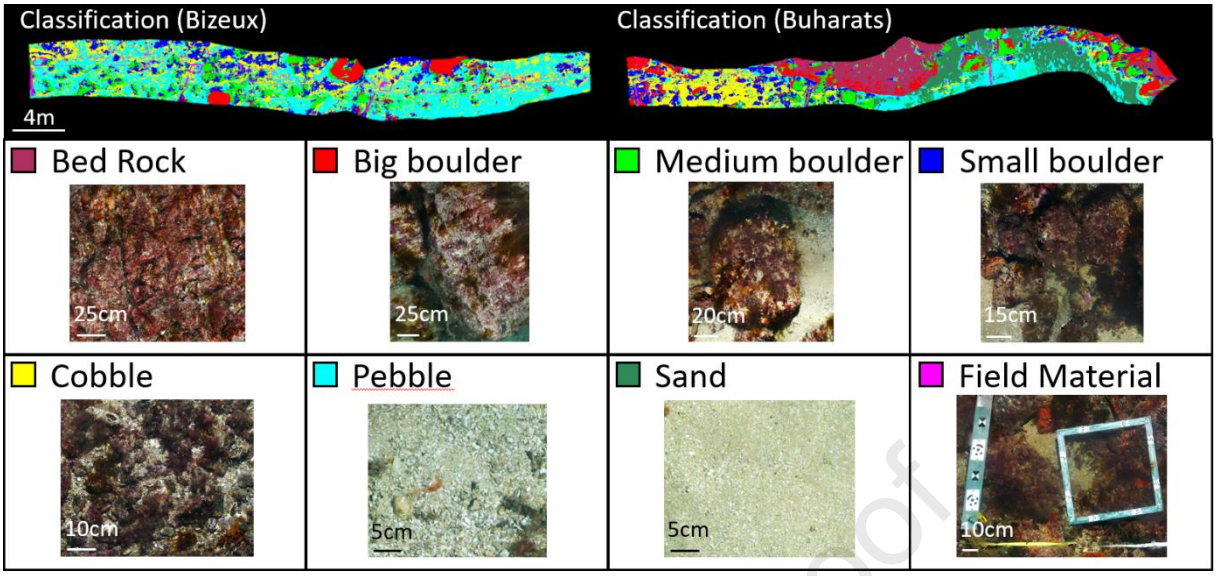

Fig.6. Classified models of transects at Bizeux and Buharats, based on multispectral (RGB), bathymetry (DSM) and all Terrain variables computed with various calculation windows. An example of each typology is given with the corresponding colour in the classification. Bed rock (homogeneous cover of rock), big (x > 1 m), medium (1 m > x > 50 cm) and small (50 cm > x > 25 cm) boulder, cobble (25 cm > x > 6 cm), pebble (6 cm > x > 4 mm), sand (4 mm > x) and field material (2 m rule, 0.25 m² quadrats and transect tape) based on Blair and McPherson (1999).

247 Each combination of variables (hereafter called processing) using the association
248 of RGB and DSM as a reference and adding Terrain for the different calculation
249 windows (1.5, 3, 6 and 9 cm) has been calculated and compared. For each classified
250 transect, a confusion matrix was generated to compare the resulting classes to the
251 validation pixel set. The matrix provided information on the accuracy of both, the
252 producer (PA; eq. 1) and the user (UA; eq. 2). The PA reflects the probability that a
253 pixel in a given class was correctly classified, while the UA expresses the probability
254 that a pixel predicted in a given class is really in that class (Congalton, 1991).
255 Consequently, the PA and UA provides information about the omission error (false
256 negative), and the commission error (false positive) respectively.

$$PA = Class_{i(Val_i)} \,/\, Val_i \times 100 \quad (1)$$

With PA (in percent), $Class_{i(Vali)}$ the number of classified pixels for the class (i) among the pixel of the validation set for the class (i), and Val_i the number of pixels of the validation set for the class (i).

$$UA = Val_{i(Class_i)} \,/\, Class_i \times 100 \quad (2)$$

With UA (in percent), $Val_{i(Classi)}$ the number of pixels of the validation set for the class (i) among the classified pixel of the class (i), and $Class_i$ the number of pixels classified for the class (i). The overall accuracy (OA), reflecting the mean quality of the classification, can then be calculated (eq. 3).

$$OA = \sum_{i=1}^{n} PA_i \,/\, n \quad (3)$$

With OA (in percent), n the total number of class and PA_i the producer's accuracy of the class (i).

2.6. Statistical analysis

The PA and UA of each processing were compared to the reference (i.e. the processing combining RGB and DSM). All statistical processes were performed using the RStudio software (version 1.4.1103; R version 4.0.4). Significance was set at a 0.05 threshold using a non-parametric Kruskal-Wallis test. A Dunn test (non-parametric pairwise comparison) was applied to detect significant variables responsible for the difference. In an exploratory way, a redundancy analysis (RDA) was conducted separately on PA and UA to show the contribution of the different variables, resolutions and kernel sizes used for the classification. A total of 27 combinations of variables was used for each site. In order to obtain these combinations, the DSM and RGB information was used as a baseline, progressively incremented with the different

Terrain variables, obtained with the different calculation windows. For each combination, the use of the different variables and calculation windows was indicated (0: not used, 1: used) as well as the accuracy (PA and UA) of each class. The significant predicted classes were selected progressively with the *ordiR2step* function of the package 'vegan'. The RDA was conducted conserving angles between variables and classes, and the significance of both the RDA and the different axes was verified using the *anova.cca* function of the package 'vegan'.

3. Results

3.1. Overview and visual description

Two DSMs were successfully produced to map the biotope on surfaces of 120 m² at a fine spatial resolution of 1 cm. The topological metrics, calculated on these areas, all indicated a high heterogeneity of the biotope in terms of morphology and substrate typology. Geomorphologically, big boulders at Bizeux (Fig. 5) are visually accompanied by high slopes, reduced maximum curvature and RMSE, and a smooth convexity. Contrastingly, small boulders, cobbles, and pebbles at Bizeux are associated with noisy slopes and convexity. The final classification, mapping the different substrate typologies, showed that the whole surface sampled area at Bizeux is covered by a mixture of boulders (bid, medium and small), cobble and pebble (Fig. 6). The final classification at Buharats showed that this site can be visually divided into 4 distinct zones, with cobbles and small boulders on the left, followed by a bed rock section, then by a pebble and sand basin, and with medium and big boulders to the right (Fig. 6).

3.2. Performances of the whole classification

307 The OA of the classification increased respectively for Bizeux and Buharats from
308 43.05 and 59.04 % when RGB and DSM are combined, to 79.54 and 84.76 % when
309 all Terrain variables (calculated with all calculation windows) are added to the
310 combination (Fig. 7).

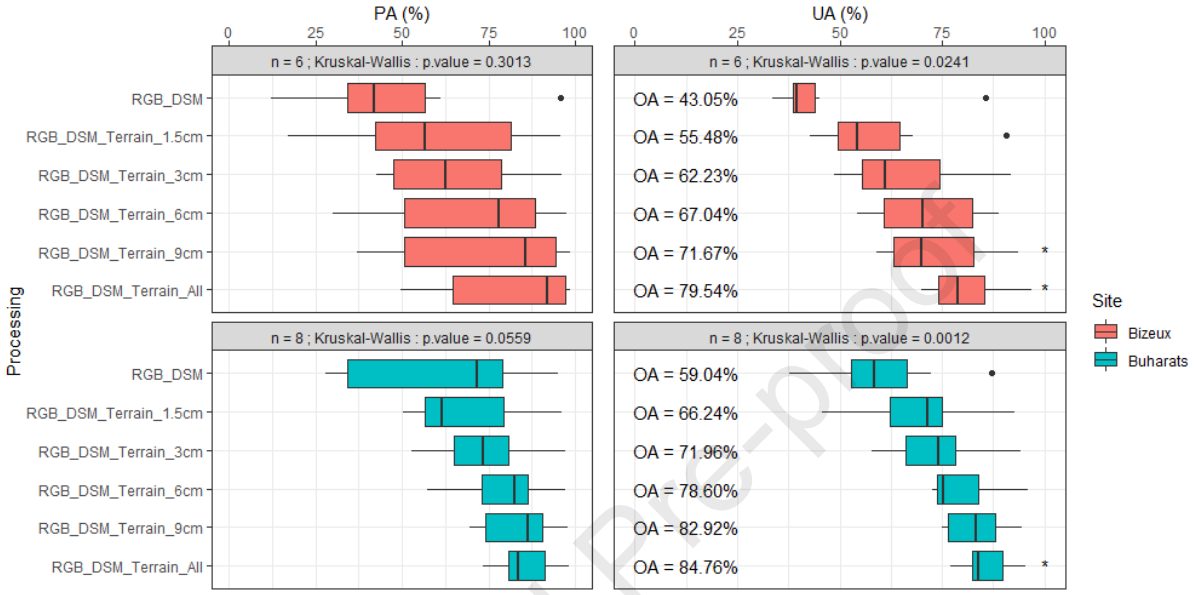

Fig.7. Boxplots (median, 25 and 75% quartiles, and outliers (dot)) showing the evolution of the accuracy of the producer (PA, left) and user (UA, right) through different processing at the sites of Bizeux (top, red) and Buharats (bottom, green). On top of each graph, the number of class used in the comparison and the p.value of the Kruskal-Wallis test are indicated. The overall accuracy (OA) is indicated for each processing. Asterisks indicate a significant difference (Dunn test, p.value < 0.05) between processing and the reference (i.e. Combination of RGB and DSM).

311 The same was observed for PA (omission error, false negative) and UA (commission
312 error, false positive). The highest PA (mean(PA_{Bizeux}) = 81.1 %, mean($PA_{Buharats}$) = 85.6
313 %) and UA (mean(UA_{Bizeux}) = 80.8 %, mean($UA_{Buharats}$) = 85.8 %) are observed when
314 all variables are combined (RGB, DSM, and Terrain calculated with all calculation
315 windows). Although the increase observed in UA is significant ($p.value_{Bizeux}$ = 0.024;

316 $p.value_{Buharats}$ = 0.001), this is not the case for PA ($p.value_{Bizeux}$ = 0.301; $p.value_{Buharats}$
317 = 0.056).

318 ## 3.3. Model performance to detect substrate classes
319

320 ### 3.3.1. Producer's accuracy (PA)
321

322 The diagonal of the confusion matrix produced highlights the concordance of
323 the classified pixel to the ground truth class. The PA showed the highest values along
324 the diagonal of the matrix for both sites when all variables are combined (RGB, DSM,
325 and Terrain calculated with all calculation windows) (Table 2). At Bizeux, most of the
326 error (wrong classified pixels) was retrieved in small boulder and cobble classes (49.64
327 and 56.34 % of well classified pixels respectively), which are both confounded with
328 medium boulder, cobble, and pebble, plus field material for cobble (grey percentages;
329 > 5.0 %) (Table 2). At Buharats, most of the error was retrieved in small boulder and
330 pebble classes (76.49 and 73.56 % of well classified pixels respectively), which are
331 confounded with medium boulder, cobble for small boulder, and cobble and sand for
332 pebble (Table 2).

333 ### 3.3.2. User's accuracy (UA)
334

335 The UA also showed the highest values along the diagonal of the matrix for
336 both sites when all variables are combined (RGB, DSM, and Terrain calculated with all
337 calculation windows; Table 3). At Bizeux, most of the error was retrieved for pebble,
338 medium boulder and cobble (70.09, 73.65 and 75.02 % of well classified pixels
339 respectively), which are confounded with small boulder and cobble (Table 3). At
340 Buharats, most of the error was observed for big boulder (76.93 % of well classified
341 pixels), which are confounded with bed rock and medium boulder (Table 3).

342 Table 2. Producer's accuracy (PA) for the different classes when all variables are combined (RGB, DSM, and Terrain calculated with
343 all calculation windows) at Bizeux (top) and Buharats (down) sites. Green and red cases highlight respectively the highest (>80 %)
344 and lowest (<80 %) percentages observed in the diagonal (classified class over ground truth class). Grey cases indicate values over
345 5.0 % (out of the diagonal).

Classified class	**Ground truth class**							
Site of Bizeux	Bed Rock	Big boulder	Medium boulder	Small boulder	Cobble	Pebble	Sand	field Material
Big boulder	/	98.13	0.45	2.4	0	0.35	/	0
Medium boulder	/	1.56	89.5	23.84	5.77	0.83	/	0.05
Small boulder	/	0.17	4.58	49.64	5	0.56	/	0.02
Cobble	/	0	1.49	13.66	56.34	3.26	/	0.7
Pebble	/	0.14	3.79	8.48	27.69	94.51	/	0.47
field Material	/	0	0.19	1.97	5.21	0.49	/	98.76
Site of Buharats	Bed Rock	Big boulder	Medium boulder	Small boulder	Cobble	Pebble	Sand	field Material
Bed Rock	82.97	0.32	0.09	0.28	0.77	1.8	0.89	0.03
Big boulder	15.04	98.22	7.76	1.57	2	1.26	1.74	0.16
Medium boulder	0.69	0.7	89.16	10.11	2.5	1.52	2.99	0.21
Small boulder	0.31	0.41	0.9	76.49	6.78	1.39	0.07	0.25
Cobble	0.44	0.06	0.52	8.13	82.2	6.29	2.07	0.22
Pebble	0.34	0.05	1.02	3.03	4.88	73.56	6.07	1.15
Sand	0.16	0	0.14	0.07	0.82	13.64	84.35	0.39
field Material	0.07	0.25	0.41	0.32	0.05	0.54	1.82	97.59

346
347
348

349 Table 3. User's accuracy (UA) for the different classes when all variables are combined (RGB, DSM, and Terrain calculated with all
350 calculation windows) at Bizeux (top) and Buharats (down) sites. Green and red cases highlight respectively the highest (>80 %) and
351 lowest (<80 %) percentages observed in the diagonal (classified class over ground truth class). Grey cases indicate values over 5.0
352 % (out of the diagonal).

Classified class	**Ground truth class**							
Site of Bizeux	Bed Rock	Big boulder	Medium boulder	Small boulder	Cobble	Pebble	Sand	field Material
Big boulder	/	96.84	0.44	2.37	0	0.35	/	0
Medium boulder	/	1.28	73.65	19.62	4.75	0.68	/	0.02
Small boulder	/	0.28	7.64	82.79	8.34	0.93	/	0.02
Cobble	/	0	1.98	18.19	75.02	4.34	/	0.47
Pebble	/	0.1	2.81	6.29	20.53	70.09	/	0.17
field Material	/	0	0.33	3.44	9.1	0.86	/	86.27
Site of Buharats	Bed Rock	Big boulder	Medium boulder	Small boulder	Cobble	Pebble	Sand	field Material
Bed Rock	95.22	0.37	0.1	0.32	0.88	2.07	1.02	0.02
Big boulder	11.78	76.93	6.08	1.23	1.57	0.99	1.36	0.06
Medium boulder	0.64	0.65	82.73	9.38	2.32	1.41	2.77	0.1
Small boulder	0.36	0.47	1.04	88.45	7.84	1.61	0.08	0.14
Cobble	0.44	0.06	0.52	8.14	82.35	6.3	2.07	0.11
Pebble	0.38	0.06	1.14	3.38	5.45	82.17	6.78	0.64
Sand	0.16	0	0.14	0.07	0.83	13.73	84.88	0.2
field Material	0.13	0.48	0.78	0.61	0.1	1.03	3.48	93.38

353

3.4. Selecting relevant variables to build relevant classifications

For both producer's (Fig. 8.1) and user's (Fig. 8.2) accuracy values, the relationship between predictors (the different Terrain variables and calculation windows) and the resulting typology was analysed by redundancy analyses (RDA).

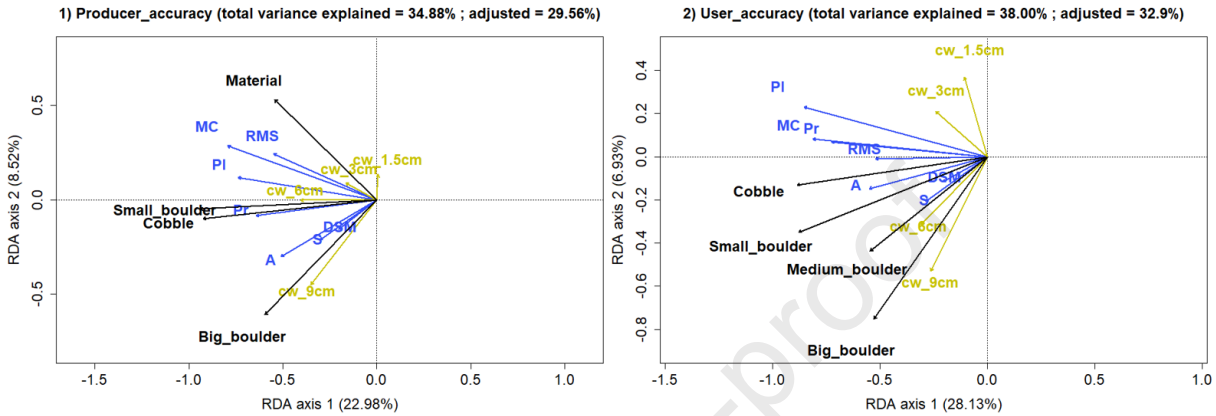

Fig. 8. Redundancy analysis (RDA) of the accuracy values of the producer (PA, graph 1) and user (UA, graph 2), showing the relationship between relevant classes (i.e. predicted typology, progressive selection; black arrows) and predictors. Predictors encompass the Terrain variables (blue) (DSM, slope (S), aspect (A), profile convexity (Pr), plan convexity (PI), maximum curvature (MC), root mean square error (RMS)) and the used calculation windows (dark yellow) (1.5 (cw_1.5cm), 3 (cw_3cm), 6 (cw_6cm), and 9 cm (cw_9cm)). Similar direction of the arrows indicates positive correlation. The total variance explained by the two significant axes (ANOVA, $p > 0.001$) is detailed in brackets for each axe. The total and adjusted variances of the RDA are indicated in brackets at the upper part of each graph.

The RDA models explained 29.56 and 32.90 % of the adjusted variance for PA and UA, respectively (Fig. 8). The progressive selection process of the PA and UA RDA models retained cobble, big and small boulder classes. The field material class was only conserved in the PA RDA model, while medium boulder was only retained in the

373 UA RDA model. Global model (integrating both axes), and the two first axes are
374 significant for PA (ANOVA; Global model: F = 6.56, p.value < 0.001; Axis 1: F = 17.29,
375 p.value < 0.001; Axis 2: F = 6.41, p.value < 0.001), and UA (ANOVA; Global model: F
376 = 7.51, p.value < 0.001; Axis 1: F = 22.23, p.value < 0.001; Axis 2: F =5.47, p.value <
377 0.001). The axis 1 highlights correlations between the Terrain variables (i.e. slope,
378 aspect, profile convexity, plan convexity, maximum curvature, RMSE, and DSM) and
379 substrate classes (i.e. big, medium, small boulder, cobble and field material) for PA
380 and UA RDA models (Fig. 8). For both of them, the axis 2 highlights positive correlation
381 between big and medium boulders for calculation windows of 6 and 9 cm, whereas
382 negative correlation is observed for calculation windows of 1.5 and 3 cm (Fig. 8).

383 # 4. Discussion
384

385 In this study, we produced a fine resolution (1 cm) classification of benthic sub-
386 tidal substrates over surfaces of 120 m² (mesoscale) of temperate reefs under
387 hydrodynamic and turbid waters using photogrammetry-based methods.

388 ## 4.1. Performance overview
389

390 Our results demonstrate that the photogrammetry approach can be used to
391 describe the substrate characteristics at scales of 120 m² with a high spatial resolution
392 of 1cm. The visual overview of the two mapping transects further highlights substrate
393 landscape differences. The Terrain variables such as slope, aspect, convexity (plan
394 and profile), maximum curvature and rugosity (RMSE) can be derived from DSM at
395 various scales. The combination of these variables with the multispectral (RGB bands)
396 information enabled a realistic and accurate (OA > 79 %) classification of the different
397 substrate typologies for both sites. Interestingly in our models, high OA were coupled
398 with high and balanced values of PA and UA, showing that substrate typological

399 classes are on average well identified (PA) and correctly predicted (UA) (Congalton,
400 1991). The highest PA and UA values were obtained when all variables were combined
401 (RGB, DSM, and Terrain calculated with all calculation windows), comforting the
402 importance of applying a multiscale approach to characterise typological classifications
403 relevant for the description of sub-tidal habitats (Wilson et al., 2007; Lecours et al.,
404 2015; Porskamp et al., 2018). In our study, variable redundancy can have added
405 statistical noise as no cross-correlation of variables was carried on. Further research
406 is thus needed to decipher the impacts of redundancy and turbidity on statistical noise.

407 Bizeux is probably one of the most turbid sites of the Emerald Coast, where
408 natural tidal currents are exacerbated by strong currents generated by the functioning
409 of the hydroelectric dam of the Rance (Gallon et al., 2013). Although, the potential high
410 turbidity observed at Bizeux does not seem to alter the quality of the DSM and
411 orthomosaic, a lower classification accuracy was obtained for Bizeux than for
412 Buharats. Despite this result, the final classification, we obtained for both sites, is
413 similar to the ones described in previous aerial imagery studies of habitat mapping of
414 land cover (James et al., 2020b), biogenic reefs (Collin et al., 2019), seagrass
415 meadows (James et al., 2020a), and macroalgae (Oppelt, 2012).

416 The multiscale approach described in this study is particularly cost/effective, as
417 the whole process from field work to the production of a high-resolution benthic
418 classification can be performed in 2 weeks. Most of the process is automatized, as the
419 computer controls for the 3D model building, Terrain variable calculations and
420 classifications, but for data acquisition and benthic classes vectorization.
421 Computational time can be saved by simplifying the classification, through grouping
422 different classes for example (e.g. big/medium/small boulder classes grouped in
423 boulders class). Subsequently, the substrate classes need careful definition regarding

the final objectives of the research, because they have a strong implication on the duration of the analysis.

4.2. Model performance to detect substrate classes

The confusion matrices indicated that field material, big and medium boulder classes appeared as the most accurately classified typologies for the two sampling sites at least for PA values. However, the worst classified typologies (low PA values) were small boulders (confused with medium boulder and cobble classes at both sites), cobble (confused with pebble at Bizeux), and pebble (confused with sand at Buharats). The UA values above 70 % reveal the concordance of the classified pixel to the ground truth class. Low UA values were observed for pebble, medium boulder and cobble at Bizeux, underlining the confusion shown for PA. Most of the confusion between classes occurred between neighbouring granulometry, which is difficult to visually distinguish during the vectorization step of the supervised classification process. A way to circumvent this could be to group the neighbouring classes, while keeping ecological relevance in terms of habitat for organisms.

4.3. Relevant variables for classification

The RDA analyses showed that the total and adjusted variances explained are quite low and are thus discussed as exploratory results needing further research. All the Terrain variables seemed to contribute to the classification of the different substrate typologies, and the larger entities (i.e. big and medium boulders) were correlated with the larger calculation windows (i.e. 6 and 9 cm). This highlights the key role of the large-scale information for the detection of large objects. Nevertheless, this scale depends on high kernel size and low resolution, having the effect to crop the borders of the sampling area and in turn reduce the classified area.

4.4. Further calculation methodologies

In this study, the maximum likelihood classifier was investigated, as it is currently used for rapid and efficient habitat descriptions (Collin et al., 2019; James et al., 2020a; James et al., 2020b). However, other machine learner classifiers can be used for supervised classification, such as random forest, support vector machine, artificial neural network (including convolutional, Collin et al., 2011) (e.g. QUEST), as well as fuzzy or unsupervised classifiers (e.g. ISODATA and k-means) (Irvin et al., 1997; Pal and Mather, 2003; Schmidt and Hewitt, 2004; Rattray et al., 2009). Testing and comparing different classifiers could be a way to choose the most appropriate process for a given site/study, refine the classification and improve its accuracy. For instance, an object based classification approach could be a relevant option, particularly for marine habitats (Wahidin et al., 2015; Ierodiaconou et al., 2018).

4.5. Access to reliefs difficult to sample

One of the perspectives of this study would be to extend this approach to other habitats, like cliffs and caves, technically difficult to characterise using LiDAR and all acoustic tools operating vertically from the surface. Studying these habitats is highly relevant since they shelter specifically adapted species, such as poriferans, ascidians and cnidarians. This is thus not surprising that these habitats are entitled “particular habitat” in the EUNIS A3.71 and A4.71 typologies (Gayet et al., 2018). Species communities, found in cliff and cave walls, are similar to the ones found at deep depths, characterised by adaptions to sciaphilic and specific oceanographic conditions and nutrient supplies (Castric-Fey et al., 1973; Bibiloni and Gili, 1989; Barnes, 1999; Meroz-Fine et al, 2005; Goffredo and Dubinsky, 2014; Sitjá and Maldonado, 2014; Quattrini et al., 2015).

4.6. Toward the characterisation of benthic communities

The photogrammetry provides pictures, that can be analysed to identify sessile organisms by photoidentification and thus further describe the benthic community associated with the different substrate types. Photoidentification is less accurate than traditional techniques, such as *in situ* identification or sampling and determination at the laboratory but could nevertheless be useful for a fast and widespread characterisation of benthic communities. In addition, photoidentification offers the possibility to test *a posteriori* the responses of communities to habitat variability, and potentially detect disturbances and their origin (human or natural).

5. Conclusion

The photogrammetry is clearly a powerful tool for a fine resolution (1cm) of the substrate characterisation at mesoscale (100 m^2 to 1 km^2). The semi-automatic classification process developed here allows now a complete description of the terrain characteristics. The georeferenced orthoprojection of the transect implemented in this study enabled to link mesoscale fine resolution information (obtained through the photogrammetric model) with a macroscale (> 1 km^2) environmental context (obtained by acoustic, LiDAR and satellite surveys). Jackson et al. (2020) and Rossi et al. (2021) also emphasized the potential of multiscale approaches to study the responses of biodiversity to environmental factors from individual to ecosystem levels using a set of complementary tools (e.g. satellites, drones, LiDAR, Sonar, AUV, ROV, Camera). This represents an innovative method for studying the relation between biological communities and their micro/macrohabitat through scales. As demonstrated in this study, the photogrammetry can be efficient even in turbid temperate water system, and is thus expected to work in a large part of sub-tidal environments. A challenge could

501 be now to develop photogrammetry for benthic community description per classes
502 based on (ortho)images that are collected to build up the classification.

Declaration of competing interest

The authors declare that they have no known competing financial interests or personal relationships that could have appeared to influence the work reported in this paper.

Acknowledgements

The authors would like to first thank Olivier Bianchimani from Semptentrion environment company for knowledge transfer in photogrammetry, allowing to explore other research perspectives at CRESCO-MNHN. Special thanks to the technical staff of the CRESCO-MNHN, in particular Julien Guillaudeau, Sébastien Aubin and Christophe Boinet, allowing the sampling campaign success with safety and with custom material. Also, thanks to Anne Lizé from CRESCO-MNHN for having proofread and corrected the English of the manuscript. Another thanks to Dorothée James, from the EPHE, for her initiation to the ENVI software. Authors are also grateful to Pertti Arvonen, from the UWIS company, for his technical support for the geolocation system. Authors finally want to thank both reviewers for taking the time to evaluate this work and providing improvements to the manuscript. This study was founded by the MARINEFF Project, developing marine infrastructure improving the ecological state of coastal water along the English Channel (Programme 2019-2022 INTERREG V-A France (Manche) - Angleterre, co-financed by the FEDER).

References

Anelli, M., Julitta, T., Fallati, L., Galli, P., Rossini, M., Colombo, R., 2017. Towards new applications of underwater photogrammetry for investigating coral reef morphology and habitat complexity in the Myeik Archipelago, Myanmar. Geocarto Int. 1–14. https://doi.org/10.1080/10106049.2017.1408703

Barnes, D.K.A., 1999. High diversity of tropical intertidal zone sponges in temperature, salinity and current extremes. Afr. J. Ecol. 37, 424–434. https://doi.org/10.1046/j.1365-2028.1999.00197.x

Bayley, D.T.I., Mogg, A.O.M., 2020. A protocol for the large-scale analysis of reefs using Structure from Motion photogrammetry. Methods Ecol. Evol. 11, 1410–1420. https://doi.org/10.1111/2041-210X.13476

Bayley, D.T.I., Mogg, A.O.M., Koldewey, H.J., Purvis, A., 2019. Capturing complexity: field-testing the use of ‘structure from motion’ derived virtual models to replicate standard measures of reef physical structure. PeerJ 1–17. https://doi.org/10.7717/peerj.6540

Bibiloni, A., Uriz, M.J., Gili, J.M., 1989. Sponge Communities in Three Submarine Caves of the Balearic Islands (Western Mediterranean): Adaptations and Faunistic Composition. Mar. Ecol. 10, 317–334.

Blair, T.C., McPherson, J.G., 1999. Grain-size and textural classification of coarse sedimentary particles. J. Sediment. Res. 69, 6–19. https://doi.org/10.2110/jsr.69.6

Bock, M., Xofis, P., Mitchley, J., Rossner, G., Wissen, M., 2005. Object-oriented methods for habitat mapping at multiple scales - Case studies from Northern

548 Germany and Wye Downs, UK. J. Nat. Conserv. 13, 75–89.
549 https://doi.org/10.1016/j.jnc.2004.12.002

550 Borland, H.P., Gilby, B.L., Henderson, C.J., Leon, J.X., Schlacher, T.A., Connolly,
551 R.M., Pittman, S.J., Sheaves, M., Olds, A.D., 2021. The influence of seafloor
552 terrain on fish and fisheries : A global synthesis. Fish Fish. 1–28.
553 https://doi.org/10.1111/faf.12546

554 Bravo, G., Livore, J.P., Bigatti, G., 2020. The Importance of Surface Orientation in
555 Biodiversity Monitoring Protocols: The Case of Patagonian Rocky Reefs. Front.
556 Mar. Sci. 7, 1–12. https://doi.org/10.3389/fmars.2020.578595

557 Brown, C.J., Smith, S.J., Lawton, P., Anderson, J.T., 2011. Benthic habitat mapping:
558 A review of progress towards improved understanding of the spatial ecology of
559 the seafloor using acoustic techniques. Estuar. Coast. Shelf Sci. 92, 502–520.
560 https://doi.org/10.1016/j.ecss.2011.02.007

561 Burns, J., Delparte, D., Gates, R., Takabayashi, M., 2015. Integrating structure-from-
562 motion photogrammetry with geospatial software as a novel technique for
563 quantifying 3D ecological characteristics of coral reefs. PeerJ 3, e1077.
564 https://doi.org/10.7717/peerj.1077

565 Burns, J.H.R., Delparte, D., Kapono, L., Belt, M., Gates, R.D., Takabayashi, M.,
566 2016. Assessing the impact of acute disturbances on the structure and
567 composition of a coral community using innovative 3D reconstruction techniques.
568 Methods Oceanogr. 15–16, 49–59. https://doi.org/10.1016/j.mio.2016.04.001

569 Calvert, J., Strong, J.A., Service, M., McGonigle, C., Quinn, R., 2015. An evaluation
570 of supervised and unsupervised classification techniques for marine benthic
571 habitat mapping using multibeam echosounder data. ICES J. Mar. Sci. 72,

572 1498–1513. https://doi.org/10.1093/icesjms/fsu223

573 Cameron, M.J., Lucieer, V., Barrett, N.S., Johnson, C.R., Edgar, G.J., 2014.
574 Understanding community-habitat associations of temperate reef fishes using
575 fine-resolution bathymetric measures of physical structure. Mar. Ecol. Prog. Ser.
576 506, 213–229. https://doi.org/10.3354/meps10788

577 Carlot, J., Rovère, A., Casella, E., Harris, D., Grellet-Muñoz, C., Chancerelle, Y.,
578 Dormy, E., Hedouin, L., Parravicini, V., 2020. Community composition predicts
579 photogrammetry-based structural complexity on coral reefs. Coral Reefs 39,
580 967–975. https://doi.org/10.1007/s00338-020-01916-8

581 Castric-Fey, A., Chasse, C., 1991. Factorial analysis in the ecology of rocky subtidal
582 areas near brest (west brittany, france). J. Mar. Biol. Assoc. United Kingdom 71,
583 515–536. https://doi.org/10.1017/S0025315400053121

584 Castric-Fey, A., Girard-Descatoire, A., Lafargue, F., L'Hardy-Halos, M.-T., 1973.
585 Etagement des algues et des invertébrés sessiles dans l'Archipel de Glénan.
586 Helgoländer wiss. Meeresunters 24, 490–509.

587 Coleman, M.A., Ingleton, T., Millar, R.B., Davies, P.L., Jordan, A., Kelaher, B.P.,
588 2016. Remotely sensed habitat variables are poor surrogates for functional traits
589 of rocky reef fish assemblages. Environ. Conserv. 43, 368–375.
590 https://doi.org/10.1017/S0376892916000205

591 Collin, A., Archambault, P., Long, B., 2011. Predicting species diversity of benthic
592 communities within turbid nearshore using full-waveform bathymetric LiDAR and
593 machine learners. PLoS One 6, 1–16.
594 https://doi.org/10.1371/journal.pone.0021265

595 Collin, A., Archambault, P., Long, B., 2008. Mapping the shallow water seabed
596 habitat with the SHOALS. IEEE Trans. Geosci. Remote Sens. 46, 2947–2955.
597 https://doi.org/10.1109/TGRS.2008.920020

598 Collin, A., Archambault, P., Planes, S., 2013. Bridging Ridge-to-Reef Patches :
599 Seamless Classification of the Coast Using Very High Resolution Satellite 5,
600 3583–3610. https://doi.org/10.3390/rs5073583

601 Collin, A., Dubois, S., James, D., Houet, T., 2019. Improving intertidal reef mapping
602 using UAV surface, red edge, and near-infrared data. Drones 3, 1–12.
603 https://doi.org/10.3390/drones3030067

604 Congalton, R.G., 1991. A review of assessing the accuracy of classifications of
605 remotely sensed data. Remote Sens. Environ. 37, 35–46.
606 https://doi.org/10.1016/0034-4257(91)90048-B

607 Diaz, R.J., Solan, M., Valente, R.M., 2004. A review of approaches for classifying
608 benthic habitats and evaluating habitat quality. J. Environ. Manage. 73, 165–
609 181. https://doi.org/10.1016/j.jenvman.2004.06.004

610 Dierssen, H.M., Theberge, A.E., 2014. Bathymetry: Assessment. Encycl. Nat.
611 Resour. Water 629–636. https://doi.org/10.1081/e-enrw-120048588

612 Duckworth, A.R., 2016. Substrate type affects the abundance and size of a coral-reef
613 sponge between depths. Mar. Freshw. Res. 67, 246–255.
614 https://doi.org/10.1071/MF14308

615 Elvenes, S., Dolan, M.F.J., Buhl-Mortensen, P., Bellec, V.K., 2014. An evaluation of
616 compiled single-beam bathymetry data as a basis for regional sediment and
617 biotope mapping. Nature 71, 867–881. https://doi.org/10.1038/278097a0

618 Ferrari, R., McKinnon, D., He, H., Smith, R.N., Corke, P., González-Rivero, M.,
619 Mumby, P.J., Upcroft, B., 2016. Quantifying multiscale habitat structural
620 complexity: A cost-effective framework for underwater 3D modelling. Remote
621 Sens. 8, 1–21. https://doi.org/10.3390/rs8020113

622 Figueira, W., Ferrari, R., Weatherby, E., Porter, A., Hawes, S., Byrne, M., 2015.
623 Accuracy and precision of habitat structural complexity metrics derived from
624 underwater photogrammetry. Remote Sens. 7, 16883–16900.
625 https://doi.org/10.3390/rs71215859

626 Fukunaga, A., Burns, J.H.R., Pascoe, K.H., Kosaki, R.K., 2020. Associations
627 between benthic cover and habitat complexity metrics obtained from 3D
628 reconstruction of coral reefs at different resolutions. Remote Sens. 12, 1–16.
629 https://doi.org/10.3390/rs12061011

630 Gallon, R.K., Ysnel, F., Feunteun, E., 2013. Optimization of an “in situ” subtidal
631 rocky-shore sampling strategy for monitoring purposes. Mar. Pollut. Bull. 74,
632 253–263. https://doi.org/10.1016/j.marpolbul.2013.06.049

633 Galparsoro, I., Guest Editor, 2012. Using EUNIS Habitat Classification for Benthic
634 Mapping in European Seas. Rev. Investig. Mar. 19, 21–70.

635 Gayet, G., Baptist, F., Maciejewski, L., Poncet, R., Bensettiti, F., 2018. Guide de
636 détermination des habitats terrestres et marins de la typologie EUNIS.

637 Goffredo, S., Dubinsky, Z., 2014. The mediterranean sea: Its history and present
638 challenges. Mediterr. Sea Its Hist. Present Challenges 1–678.
639 https://doi.org/10.1007/978-94-007-6704-1

640 Guinan, J., Grehan, A.J., Dolan, M.F.J., Brown, C., 2009. Quantifying relationships

641 between video observations of cold-water coral cover and seafloor features in
642 rockall trough, west of Ireland. Mar. Ecol. Prog. Ser. 375, 125–138.
643 https://doi.org/10.3354/meps07739

644 Hasan, R.C., Ierodiaconou, D., Laurenson, L., Schimel, A., 2014. Integrating
645 multibeam backscatter angular response, mosaic and bathymetry data for
646 benthic habitat mapping. PLoS One 9, 1–14.
647 https://doi.org/10.1371/journal.pone.0097339

648 Hatcher, G.A., Warrick, J.A., Ritchie, A.C., Dailey, E.T., Zawada, D.G., Kranenburg,
649 C., Yates, K.K., 2020. Accurate Bathymetric Maps From Underwater Digital
650 Imagery Without Ground Control. Front. Mar. Sci. 7, 1–20.
651 https://doi.org/10.3389/fmars.2020.00525

652 Holmes, K.W., Van Niel, K.P., Radford, B., Kendrick, G.A., Grove, S.L., 2008.
653 Modelling distribution of marine benthos from hydroacoustics and underwater
654 video. Cont. Shelf Res. 28, 1800–1810. https://doi.org/10.1016/j.csr.2008.04.016

655 Ierodiaconou, D., Schimel, A.C.G., Kennedy, D., Monk, J., Gaylard, G., Young, M.,
656 Diesing, M., Rattray, A., 2018. Combining pixel and object based image analysis
657 of ultra-high resolution multibeam bathymetry and backscatter for habitat
658 mapping in shallow marine waters. Mar. Geophys. Res. 39, 271–288.
659 https://doi.org/10.1007/s11001-017-9338-z

660 Irish, J.L., Lillycrop, W.J., 1999. Scanning laser mapping of the coastal zone: The
661 SHOALS system. ISPRS J. Photogramm. Remote Sens. 54, 123–129.
662 https://doi.org/10.1016/S0924-2716(99)00003-9

663 Irvin, B.J., Ventura, S.J., Slater, B.K., 1997. Fuzzy and isodata classification of
664 landform elements from digital terrain data in Pleasant Valley, Wisconsin.

665 Geoderma 77, 137–154. https://doi.org/10.1016/S0016-7061(97)00019-0

666 Jackson, T.D.U., Williams, G.J., Walker-springett, G., Davies, A.J., 2020. Three-
667 dimensional digital mapping of ecosystems : a new era in spatial ecology. Proc.
668 R. Soc. B 287, 1–10. https://doi.org/10.1098/rspb.2019.2383

669 James, Dorothée, Collin, A., Houet, T., Mury, A., Gloria, H., Le, N., 2020. Towards
670 Better Mapping of Seagrass Meadows using UAV Multispectral and Topographic
671 Data. J. co 95, 1117–1121. https://doi.org/10.2112/SI95-217.1

672 James, D., Collin, A., Mury, A., Costa, S., 2020. Very high resolution land use and
673 land cover mapping using pleiades-1 stereo imagery and machine learning. Int.
674 Arch. Photogramm. Remote Sens. Spat. Inf. Sci. - ISPRS Arch. 43, 675–682.
675 https://doi.org/10.5194/isprs-archives-XLIII-B2-2020-675-2020

676 Keith, D.A., Ferrer-paris, J.R., Nicholson, E., Kingsford, R.T., 2020. IUCN Global
677 Ecosystem Typology 2.0: descriptive profiles for biomes and ecosystem
678 functional groups. Gland, Switzerland.
679 https://doi.org/10.2305/iucn.ch.2020.13.en

680 Knudby, A., LeDrew, E., Brenning, A., 2010. Predictive mapping of reef fish species
681 richness, diversity and biomass in Zanzibar using IKONOS imagery and
682 machine-learning techniques. Remote Sens. Environ. 114, 1230–1241.
683 https://doi.org/10.1016/j.rse.2010.01.007

684 Knudby, A., Roelfsema, C., Lyons, M., Phinn, S., Jupiter, S., 2011. Mapping fish
685 community variables by Integrating field and satellite data, object-based image
686 analysis and modeling in a traditional Fijian fisheries management area. Remote
687 Sens. 3, 460–483. https://doi.org/10.3390/rs3030460

688 Kuffner, I.B., Brock, J.C., Grober-Dunsmore, R., Bonito, V.E., Hickey, T.D., Wright,
689 C.W., 2007. Relationships between reef fish communities and remotely sensed
690 rugosity measurements in Biscayne National Park, Florida, USA. Environ. Biol.
691 Fishes 78, 71–82. https://doi.org/10.1007/s10641-006-9078-4

692 Lecours, V., Devillers, R., Schneider, D.C., Lucieer, V.L., Brown, C.J., Edinger, E.N.,
693 2015. Spatial scale and geographic context in benthic habitat mapping: Review
694 and future directions. Mar. Ecol. Prog. Ser. 535, 259–284.
695 https://doi.org/10.3354/meps11378

696 Leon, J.X., Roelfsema, C.M., Saunders, M.I., Phinn, S.R., 2015. Measuring coral reef
697 terrain roughness using “Structure-from-Motion” close-range photogrammetry.
698 Geomorphology 242, 21–28. https://doi.org/10.1016/j.geomorph.2015.01.030

699 Madricardo, F., Foglini, F., Campiani, E., Grande, V., Catenacci, E., Petrizzo, A.,
700 Kruss, A., Toso, C., Trincardi, F., 2019. Assessing the human footprint on the
701 sea-floor of coastal systems: the case of the Venice Lagoon, Italy. Sci. Rep. 9,
702 1–14. https://doi.org/10.1038/s41598-019-43027-7

703 Marre, G., De Almeida Braga, C., Ienco, D., Luque, S., Holon, F., Deter, J., 2020a.
704 Deep convolutional neural networks to monitor coralligenous reefs:
705 Operationalizing biodiversity and ecological assessment. Ecol. Inform. 59,
706 101110. https://doi.org/10.1016/j.ecoinf.2020.101110

707 Marre, G., Deter, J., Holon, F., Boissery, P., Luque, S., 2020b. Fine-scale automatic
708 mapping of living posidonia oceanica seagrass beds with underwater
709 photogrammetry. Mar. Ecol. Prog. Ser. 643, 63–74.
710 https://doi.org/10.3354/meps13338

711 Marre, G., Holon, F., Luque, S., Boissery, P., Deter, J., 2019. Monitoring Marine

712 Habitats With Photogrammetry: A Cost-Effective, Accurate, Precise and High-
713 Resolution Reconstruction Method. Front. Mar. Sci. 6, 1–15.
714 https://doi.org/10.3389/fmars.2019.00276

715 Meroz-Fine, E., Shefer, S., Ilan, M., 2005. Changes in morphology and physiology of
716 an East Mediterranean sponge in different habitats. Mar. Biol. 147, 243–250.
717 https://doi.org/10.1007/s00227-004-1532-2

718 Monk, J., Ierodiaconou, D., Bellgrove, A., Harvey, E., Laurenson, L., 2011. Remotely
719 sensed hydroacoustics and observation data for predicting fish habitat suitability.
720 Cont. Shelf Res. 31, 17–27. https://doi.org/10.1016/j.csr.2010.02.012

721 Monk, J., Ierodiaconou, D., Versace, V.L., Bellgrove, A., Harvey, E., Rattray, A.,
722 Laurenson, L., Quinn, G.P., 2010. Habitat suitability for marine fishes using
723 presence-only modelling and multibeam sonar. Mar. Ecol. Prog. Ser. 420, 157–
724 174. https://doi.org/10.3354/meps08858

725 Moore, C.H., Harvey, E.S., Van Niel, K., 2010. The application of predicted habitat
726 models to investigate the spatial ecology of demersal fish assemblages. Mar.
727 Biol. 157, 2717–2729. https://doi.org/10.1007/s00227-010-1531-4

728 Moore, C.H., Harvey, E.S., Van Niel, K.P., 2009. Spatial prediction of demersal fish
729 distributions: Enhancing our understanding of species-environment relationships.
730 ICES J. Mar. Sci. 66, 2068–2075. https://doi.org/10.1093/icesjms/fsp205

731 Oppelt, N., 2012. Hyperspectral classification approaches for intertidal macroalgae
732 habitat mapping: a case study in Heligoland. Opt. Eng. 51, 111703.
733 https://doi.org/10.1117/1.oe.51.11.111703

734 Pal, M., Mather, P.M., 2003. An assessment of the effectiveness of decision tree

methods for land cover classification. Remote Sens. Environ. 86, 554–565. https://doi.org/10.1016/S0034-4257(03)00132-9

Pickrill, R.A., Todd, B.J., 2003. The multiple roles of acoustic mapping in integrated ocean management, Canadian Atlantic continental margin. Ocean Coast. Manag. 46, 601–614. https://doi.org/10.1016/S0964-5691(03)00037-1

Pittman, S.J., Brown, K.A., 2011. Multi-scale approach for predicting fish species distributions across coral reef seascapes. PLoS One 6, 1–12. https://doi.org/10.1371/journal.pone.0020583

Pittman, S.J., Christensen, J.D., Caldow, C., Menza, C., Monaco, M.E., 2007. Predictive mapping of fish species richness across shallow-water seascapes in the Caribbean. Ecol. Modell. 204, 9–21. https://doi.org/10.1016/j.ecolmodel.2006.12.017

Pittman, S.J., Costa, B.M., Battista, T.A., 2009. Using Lidar Bathymetry and Boosted Regression Trees to Predict the Diversity and Abundance of Fish and Corals. J. Coast. Res. 10053, 27–38. https://doi.org/10.2112/si53-004.1

Porskamp, P., Rattray, A., Young, M., Ierodiaconou, D., 2018. Multiscale and hierarchical classification for benthic habitat mapping. Geosciences 8, 1–24. https://doi.org/10.3390/geosciences8040119

Pygas, D.R., Ferrari, R., Figueira, W.F., 2020. Review and meta-analysis of the importance of remotely sensed habitat structural complexity in marine ecology. Estuar. Coast. Shelf Sci. 235, 1–16. https://doi.org/10.1016/j.ecss.2019.106468

Quattrini, A.M., Nizinski, M.S., Chaytor, J.D., Demopoulos, A.W.J., Roark, E.B., France, S.C., Moore, J.A., Heyl, T., Auster, P.J., Kinlan, B., Ruppel, C., Elliott,

758 K.P., Kennedy, B.R.C., Lobecker, E., Skarke, A., Shank, T.M., 2015. Exploration
759 of the canyon-incised continental margin of the northeastern United States
760 reveals dynamic habitats and diverse communities. PLoS One 10, 1–32.
761 https://doi.org/10.1371/journal.pone.0139904

762 Rattray, A., Ierodiaconou, D., Laurenson, L., Burq, S., Reston, M., 2009. Hydro-
763 acoustic remote sensing of benthic biological communities on the shallow South
764 East Australian continental shelf. Estuar. Coast. Shelf Sci. 84, 237–245.
765 https://doi.org/10.1016/j.ecss.2009.06.023

766 Rees, M.J., Knott, N.A., Neilson, J., Linklater, M., Osterloh, I., Jordan, A., Davis, A.R.,
767 2018. Accounting for habitat structural complexity improves the assessment of
768 performance in no-take marine reserves. Biol. Conserv. 224, 100–110.
769 https://doi.org/10.1016/j.biocon.2018.04.040

770 Rossi, P., Ponti, M., Righi, S., Castagnetti, C., Simonini, R., Mancini, F., Agrafiotis,
771 P., Bassani, L., Bruno, F., Cerrano, C., Cignoni, P., Corsini, M., Drap, P.,
772 Dubbini, M., Garrabou, J., Gori, A., Gracias, N., Ledoux, J.B., Linares, C.,
773 Mantas, P.T., Menna, F., Nocerino, E., Palma, M., Pavoni, G., Ridolfi, A., Rossi,
774 S., Skarlatos, D., Treibitz, T., Turicchia, E., Yuval, M., Capra, A., 2021. Needs
775 and Gaps in Optical Underwater Technologies and Methods for the Investigation
776 of Marine Animal Forest 3D-Structural Complexity. Front. Mar. Sci. 8, 1–9.
777 https://doi.org/10.3389/fmars.2021.591292

778 Schmidt, J., Hewitt, A., 2004. Fuzzy land element classification from DTMs based on
779 geometry and terrain position. Geoderma 121, 243–256.
780 https://doi.org/10.1016/j.geoderma.2003.10.008

781 Sekund, L., Pittman, S., 2017. Explaining island-wide geographical patterns of

782 Caribbean fish diversity: A multi-scale seascape ecology approach. Mar. Ecol.
783 38, 1–19. https://doi.org/10.1111/maec.12434

784 Sitjá, C., Maldonado, M., 2014. New and rare sponges from the deep shelf of the
785 Alboran Island (Alboran Sea, Western Mediterranean). Zootaxa 3760, 141–179.
786 https://doi.org/10.11646/zootaxa.3760.2.2

787 Smith, G., Yesilnacar, E., Jiang, J., Taylor, C., 2015. Marine habitat mapping
788 incorporating both derivatives of LiDAR data and hydrodynamic conditions. J.
789 Mar. Sci. Eng. 3, 492–508. https://doi.org/10.3390/jmse3030492

790 Wahidin, N., Siregar, V.P., Nababan, B., Jaya, I., Wouthuyzen, S., 2015. Object-
791 based Image Analysis for Coral Reef Benthic Habitat Mapping with Several
792 Classification Algorithms. Procedia Environ. Sci. 24, 222–227.
793 https://doi.org/10.1016/j.proenv.2015.03.029

794 Walbridge, S., Slocum, N., Pobuda, M., Wright, D.J., 2018. Unified geomorphological
795 analysis workflows with benthic terrain modeler. Geosciences 8, 1–24.
796 https://doi.org/10.3390/geosciences8030094

797 Williams, J., Jordan, A., Harasti, D., Davies, P., Ingleton, T., 2019. Taking a deeper
798 look: Quantifying the differences in fish assemblages between shallow and
799 mesophotic temperate rocky reefs. PLoS One 14, 1–20.
800 https://doi.org/10.1101/449959

801 Wilson, M.F.J., O'Connell, B., Brown, C., Guinan, J.C., Grehan, A.J., 2007. Multiscale
802 terrain analysis of multibeam bathymetry data for habitat mapping on the
803 continental slope. Mar. Geod. 30, 3–35.
804 https://doi.org/10.1080/01490410701295962

805 Zavalas, R., Ierodiaconou Daniel, D., Ryan, D., Rattray, A., Monk, J., 2014. Habitat
806 classification of temperate marine macroalgal communities using bathymetric
807 LiDAR. Remote Sens. 6, 2154–2175. https://doi.org/10.3390/rs6032154

808

Table 1: The different combinations of resolution (r) and kernel size (k) to obtain the different calculation windows

Calculation window (in cm)	Kernel size (k, in pixel)	Resolution (r, in mm)
1.5	30	5
3	30	10
6	60	10
9	90	10

Table 2. Producer's accuracy (PA) for the different classes when all variables are combined (RGB, DSM, and Terrain calculated with all calculation windows) at Bizeux (top) and Buharats (down) sites. Green and red cases highlight respectively the highest (>80 %) and lowest (<80 %) percentages observed in the diagonal (classified class over ground truth class). Grey cases indicate values over 5.0 % (out of the diagonal).

Classified class	**Ground truth class**							
Site of Bizeux	Bed Rock	Big boulder	Medium boulder	Small boulder	Cobble	Pebble	Sand	field Material
Big boulder	/	98.13	0.45	2.4	0	0.35	/	0
Medium boulder	/	1.56	89.5	23.84	5.77	0.83	/	0.05
Small boulder	/	0.17	4.58	49.64	5	0.56	/	0.02
Cobble	/	0	1.49	13.66	56.34	3.26	/	0.7
Pebble	/	0.14	3.79	8.48	27.69	94.51	/	0.47
field Material	/	0	0.19	1.97	5.21	0.49	/	98.76
Site of Buharats	Bed Rock	Big boulder	Medium boulder	Small boulder	Cobble	Pebble	Sand	field Material
Bed Rock	82.97	0.32	0.09	0.28	0.77	1.8	0.89	0.03
Big boulder	15.04	98.22	7.76	1.57	2	1.26	1.74	0.16
Medium boulder	0.69	0.7	89.16	10.11	2.5	1.52	2.99	0.21
Small boulder	0.31	0.41	0.9	76.49	6.78	1.39	0.07	0.25
Cobble	0.44	0.06	0.52	8.13	82.2	6.29	2.07	0.22
Pebble	0.34	0.05	1.02	3.03	4.88	73.56	6.07	1.15
Sand	0.16	0	0.14	0.07	0.82	13.64	84.35	0.39
field Material	0.07	0.25	0.41	0.32	0.05	0.54	1.82	97.59

Table 3. User's accuracy (UA) for the different classes when all variables are combined (RGB, DSM, and Terrain calculated with all calculation windows) at Bizeux (top) and Buharats (down) sites. Green and red cases highlight respectively the highest (>80 %) and lowest (<80 %) percentages observed in the diagonal (classified class over ground truth class). Grey cases indicate values over 5.0 % (out of the diagonal).

Classified class	**Ground truth class**							
Site of Bizeux	Bed Rock	Big boulder	Medium boulder	Small boulder	Cobble	Pebble	Sand	field Material
Big boulder	/	96.84	0.44	2.37	0	0.35	/	0
Medium boulder	/	1.28	73.65	19.62	4.75	0.68	/	0.02
Small boulder	/	0.28	7.64	82.79	8.34	0.93	/	0.02
Cobble	/	0	1.98	18.19	75.02	4.34	/	0.47
Pebble	/	0.1	2.81	6.29	20.53	70.09	/	0.17
field Material	/	0	0.33	3.44	9.1	0.86	/	86.27
Site of Buharats	Bed Rock	Big boulder	Medium boulder	Small boulder	Cobble	Pebble	Sand	field Material
Bed Rock	95.22	0.37	0.1	0.32	0.88	2.07	1.02	0.02
Big boulder	11.78	76.93	6.08	1.23	1.57	0.99	1.36	0.06
Medium boulder	0.64	0.65	82.73	9.38	2.32	1.41	2.77	0.1
Small boulder	0.36	0.47	1.04	88.45	7.84	1.61	0.08	0.14
Cobble	0.44	0.06	0.52	8.14	82.35	6.3	2.07	0.11
Pebble	0.38	0.06	1.14	3.38	5.45	82.17	6.78	0.64
Sand	0.16	0	0.14	0.07	0.83	13.73	84.88	0.2
field Material	0.13	0.48	0.78	0.61	0.1	1.03	3.48	93.38

Graphical Abstract

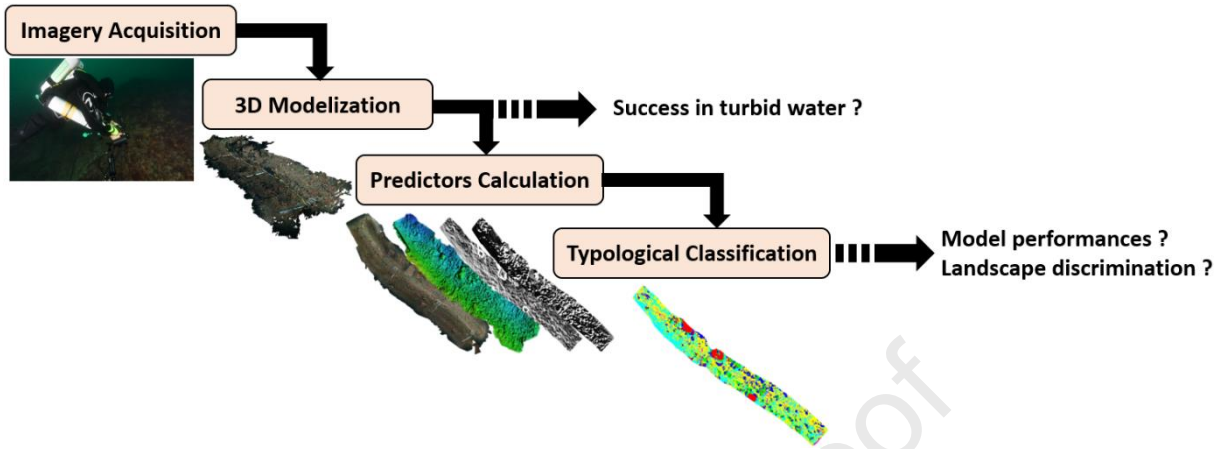

Highlights

• Photogrammetric technique is applicable for high resolution (~1cm) mesoscale (~100m²) benthic temperate reef characterization in turbid coastal waters.

• Supervised classification provides good performance for benthic substrate mapping at a centimetre resolution.

• Resulting maps enable detection of landscape variability within and between sites.

Authors agreement to the submission

All authors declare being agree to the submission

Author contributions

Quentin Ternon, Éric Feunteun, Frédéric Ysnel, Pierre Thiriet and Antoine Collin developed the study approach.

Quentin Ternon and Valentin Danet collected the data.

Quentin Ternon and Antoine Collin conducted the data analysis.

Quentin Ternon wrote the paper.

All authors participated to the manuscript revision.

Antoine Collin supervised the research.

Declaration of interests

☒ The authors declare that they have no known competing financial interests or personal relationships that could have appeared to influence the work reported in this paper.

☐ The authors declare the following financial interests/personal relationships which may be considered as potential competing interests: